Brodogradnja Volume 75, Number 1 (2024) 75102

journal homepage: www.brodogradnja.fsb.hr

Brodogradnja

An International Journal of Naval Architecture and Ocean Engineering for Research and Development

On the propeller wake evolution using large eddy simulations and physics-informed space-time decomposition

Zhan Zhang[1,2,3], *Peng Sun*[1,2,3]*, *Long Pan*[4], *Teng Zhao*[5]

[1] *Chongqing Southwest Research Institute for Water Transport Engineering, Chongqing Jiaotong University*
[2] *Key Laboratory of Inland Waterway Regulation Engineering, Chongqing Jiaotong University*
[3] *Chongqing Xike Water Transport Engineering Consulting Co., Ltd*
[4] *Bomber and Transport Aircraft Pilots Conversion Department*
[5] *School of Shipping and Naval Architecture, Chongqing Jiaotong University*

ARTICLE INFO

Editor-in-Chief: Prof. Nastia Degiuli
Associate Editor: PhD Ivana Martić

Keywords:
LES
Pi-SPDMD
Numerical analysis
Propeller wakes
Tip vortex instability
Vorticity

ABSTRACT

A novel modal analysis methodology, denoted as the physics informed sparsity-promoting dynamic mode decomposition (pi-SPDMD) model, was introduced for the reduction and reconstruction analysis of intricate propeller wake flows, aiming to provide insight into the inherent flow structures spanning diverse temporal and spatial scales. Large-Eddy Simulation (LES) was employed to numerically model the wake dynamics of a four-bladed propeller, providing a comprehensive resolution from the proximate to the distant wake regions. The findings indicate that the pi-SPDMD model enhances the efficiency of the sparse-promoting algorithm, producing modes that gravitate towards stability, and the resulting decomposition maintains commendable physical fidelity. Integrating the results from the LES solution and the modal decomposition of pi-SPDMD, the tip vortex exhibits a uniform topological configuration with notable coherence in the proximate domain. In this region, the large-scale vortex is the dominant feature of the propeller wake, and there is a marked intermittency in the turbulence. In the mid-field, the tip vortex system transitions into fine-scale vortices, rapidly diminishing in coherence due to the onset of elliptic instability and subsequent secondary vortex generation. As the tip vortex structures related to physical quantities become fully discretized, the small-scale turbulent patterns quickly intermingle, leading to a more homogeneous distribution in the distant wake.

1. Introduction

The turbulent characteristics of propeller wake represent a pivotal domain within fluid dynamics research. As propellers operate within aqueous or aerial environments, they engender intricate flow dynamics. The turbulence evident in propeller wakes predominantly emanates from shear interactions between the propeller blades and the ambient fluid. As the rotational speed of the propeller escalates, the velocity of the fluid passing over the blades concomitantly rises, intensifying the shear stress between the fluid and the blades, which subsequently culminates in turbulence formation. Each blade of the propeller, during rotation, generates

* Corresponding author.
E-mail address: sunpeng@cqjtu.edu.cn

http://dx.doi.org/10.21278/brod75102
Submitted 31 October 2023; Accepted 01 November 2023;
ISSN 0007-215X; eISSN 1845-5859

vortices, which interact with the wake, further amplifying the turbulence attributes [1-7]. Under specific conditions, cavitation bubbles might manifest in the propeller wake. This phenomenon transpires when, with the augmentation of fluid velocity, there's a concomitant decline in pressure, potentially leading to vapor formation within the fluid. These bubbles, during their transit, might undergo implosion, yielding noise and vibrations. Turbulence can detrimentally impinge upon the efficiency and overall performance of vessels. It has the potential to augment drag, compromise propeller efficiency, and induce erosion on the propeller's surface. In summation, the turbulent characteristics intrinsic to the propeller wake hold significant ramifications for a vessel's performance, efficiency, and longevity. Hence, an in-depth exploration of this sphere is paramount for enhancing marine vessel performance and attenuating environmental repercussions [8-12].

For surface ships and underwater vehicles, propellers serve as the primary propulsion mechanism. Analyzing the flow within a marine propeller's wake is crucial due to its significant impact on noise, vibration, and overall propulsion efficiency [13-17]. A comprehensive understanding is imperative for developing next-generation propellers with enhanced performance and for improving existing designs. Yet, the complex turbulent flow patterns in the propeller wake incorporate diverse evolutionary mechanisms that are predominantly enigmatic. Specifically, the physical underpinnings of complex events like elliptical (short-wave) instability and tip vortex merging are not entirely grasped [18-24]. Focusing on wake instabilities, this study aims to elucidate the mechanisms underlying the evolution of propeller wakes.

Several experimental studies have delved into the instability of propeller wakes. Di Felice et al. [25] employed particle image velocimetry (PIV) enhanced by an iterative window offset and stretching technique within a cavitation tunnel to examine propeller wake dynamics. Key characteristics of the propeller wake were identified under diverse loading scenarios. Later, Felli et al. [26] explored the progression of both propeller tip and hub vortices from transitional areas to the far field using time-resolved visualizations and velocimetry assessments. Their findings underscored that wake instability was influenced by the inter-spiral spacing, notably highlighting a streamwise shift in the transition region with increased inter-spiral distances. Mukund and Kumar [27] conducted low-speed wind tunnel tests on an isolated powered propeller model, employing two-component hot-wire anemometry to ascertain the velocity field in the plane behind the propeller. They discerned that transition might occur near the wing's leading edge, positioning it as a prime candidate for optimization. Using a multi-camera PIV setup, Felli and Falchi [28] investigated wake flow behind an isolated propeller in oblique flow. Their comparative analysis illuminated distinct wake behaviors under various conditions, emphasizing the substantial hydrodynamic effects of non-axisymmetric conditions on wake evolution mechanisms. In a subsequent study in 2020, Felli and Falchi [29] explored the temporal dimensions of the primary mechanisms influencing vortex dynamics, utilizing phase-locked imagery and averaging methods derived from an extensive test matrix. Their research shed light on the onset of wake instability and the multifaceted progression of tip vortex interactions, including its association with the hub vortex.

Various numerical studies have delved into the evolution of propeller wake under diverse conditions. Muscari et al. [18] examined the flow around a rotating marine propeller, aiming to discern the strengths and weaknesses of various turbulence modeling strategies. In evaluating several eddy viscosity models, they found the RANSE method proficient in predicting global quantities, though it tended to be overly dissipative during instability processes. Leveraging large eddy simulation, Kumar and Mahesh [30] probed the wake of a five-bladed maritime propeller operating under design-specific loading conditions. Their findings spotlighted a mutual-induction instability mechanism wherein tip vortices engaged with finer vortices formed by the roll-up of blade trailing edge wake in the proximate wake, rather than interactions solely between tip vortices. Li et al. [31] examined the wake characteristics of a pump-jet propulsor (PJP) equipped with a pre-swirl stator using stress-blended eddy simulations, offering a methodical assessment of wake configurations under varied loading scenarios. Their findings indicated a minimal correlation between tip clearance leakage vortices and hub vortex instability. Meanwhile, Wang et al. [32] analyzed the propeller wake using an enhanced delayed detached eddy simulation, applying flow decomposition techniques under different loadings. Their research suggested that the circumferential dispersion of the tip vortex structure facilitates the convergence of adjacent tip vortices.

In large eddy simulations (LES), only the turbulence motions with the highest energy densities are directly resolved, with the effects of the finer, unresolved scales being modeled. This methodology has been implemented in studies concerning propeller wakes. Kumar and Mahesh [30] employed LES to investigate the wake dynamics of a five-bladed maritime propeller under specified design load conditions. The research unveils a novel mechanism of mutual-induction effect, wherein the interplay between tip vortices and strong trailing-edge vortices also precipitates instability. Posa [33] utilized LES to simulate the wake evolution processes of both tip-loaded propeller and conventional propeller under designed advance coefficient conditions. The results indicate that compared to conventional propellers, the two tip vortices generated by the blades of the tip-loaded propeller rapidly merge, subsequently delaying the instability progression of wake evolution. This research provides new insights for the design of tip-loaded propellers. Posa et al. [34] employed LES to analyze the dynamic characteristics of the propeller tip vortices and hub vortices from both Eulerian and Lagrangian perspectives. They elucidated the evolution process of the wake vortex system in detail, emphasizing the roles played by the tip vortices and hub vortices in the aforementioned instability progression. For a deeper understanding of LES theory and its applications, readers are directed to relevant references [35-38].

Modal decomposition techniques are extensively utilized in fluid mechanics and turbulence research. These techniques are particularly relevant in examining turbulent mechanisms and the progression of propeller wake dynamics, the data associated with turbulence is often intricate, encompassing a wealth of information [39]. Through modal decomposition, we can identify modes that best represent the dynamics of the flow field, thereby achieving effective data dimensionality reduction. Modal decomposition techniques adeptly extract predominant fluid dynamic features and structures from complex flow field data, such as large vortex structures and wake patterns. By analyzing various modes, researchers can gain a more profound understanding of the genesis, development, and decay mechanisms of turbulence or wakes, providing a theoretical foundation for turbulence control and optimization. Techniques like DMD, in particular, offer an in-depth understanding of spatial patterns and temporal dynamics, thus revealing the temporal and spatial evolution characteristics of flows. In sum, modal decomposition techniques serve as a potent tool for the study of turbulence and the evolution of propeller wakes, effectively extracting critical information from vast datasets, thereby furnishing theoretical support for fluid machinery design and optimization [40].

While numerous studies have explored propeller wake attributes under diverse scenarios, there is a noticeable gap in detailed numerical investigations employing both the LES turbulence model and modal decomposition techniques. Leveraging the LES approach alongside a newly proposed pi-SPDMD model, this study offers an exhaustive analysis of flow dynamics across the complete spectrum of a propeller wake evolution, specifically under moderate loading conditions. This research not only uncovers mechanisms underlying the destabilization of the propeller wake but also holds potential to inform and refine designs of future-generation propellers.

2. Research model

The propeller model under consideration, E779A, is a four-bladed, fixed-pitch, low-skew right-handed design. The propeller diameter is 0.227m. Previous extensive studies on the E779A propeller can be found in works by Wang et al. [41-42]. The referenced works include both numerical simulations and experimental data. Figure 1 displays the E779A propeller's geometric model alongside its reference system.

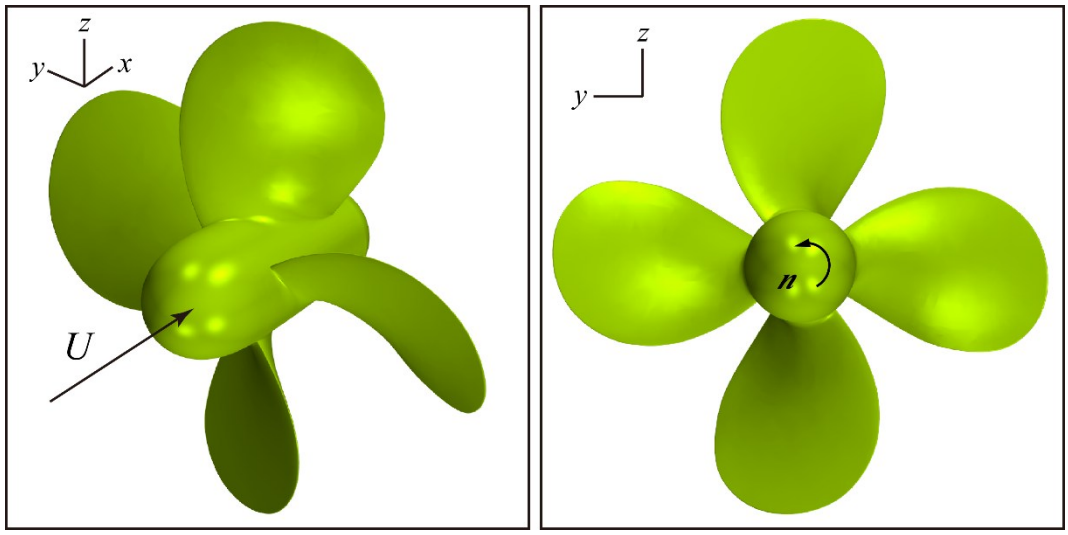

Fig. 1. E779A propeller and reference system.

3. Numerical simulations

3.1 Numerical method

The propeller wake turbulent structures are captured using the LES method, a transient numerical technique where equations undergo spatial filtering. Large-scale turbulence is directly addressed, while small-scale eddies are represented via the subgrid-scale (SGS) model within the LES framework [43]. This study utilizes implicit filtering, an efficient computational approach that maximizes grid resolution, determining the eddy scales filtered by the computational grid. The Wall-Adapting Local-Eddy Viscosity (WALE) SGS model is selected for simulation. Unlike traditional models like Smagorinsky's, the modern WALE SGS model, built on a unique velocity gradient tensor, minimizes sensitivity to model coefficient values and obviates the need for near-wall damping, offering precise scaling at solid wall boundaries. The WALE SGS model's efficacy in marine hydrodynamics has garnered consistent validation [44-45]. LES has been extensively applied in studying propeller wake instabilities [46]. The equations are as follows:

$$\nabla \cdot \boldsymbol{u} = 0 \tag{1}$$

$$\frac{\partial \boldsymbol{u}}{\partial t} + \nabla \cdot \boldsymbol{u}\boldsymbol{u} = -\nabla \tilde{p} - \nabla \cdot \boldsymbol{\tau} + \frac{1}{Re}\nabla^2 \boldsymbol{u} \tag{2}$$

where $\boldsymbol{u}$ is the filtered velocity vector, $\tilde{p}$ is the filtered pressure, t is the time variable, $\boldsymbol{\tau}$ is the subgrid scale stress tensor and Re is the Reynolds number.

In this study, the LES simulation employs the open-source CFD software OpenFOAM [47-48]. The designated time step is 1.1111×10^{-4} s, equivalent to a 1° propeller rotation. Spatial and temporal discretizations are performed using second-order schemes to ensure numerical accuracy. Specifically, the convection term is discretized via an upwind differencing approach, while the diffusion term employs a central scheme. Additionally, the transient term is addressed through a backward implicit method in the temporal domain.

3.2 Physics-informed Sparsity-promoting Dynamic Mode Decomposition (pi-SPDMD)

Initially, m snapshots are collected from the flow field. These representative snapshots correspond to each time step of the flow field and are reassembled into a column vector. In this study, this state vector is defined as:

$$x_k = \left[u(t_k)^T \quad v(t_k)^T \quad w(t_k)^T \right] \in \mathbb{R}^{n\times 1} \tag{3}$$

wherein, $u(t_k)$, $v(t_k)$, $w(t_k)$ respectively represent the vectorized velocity field components in three directions at time t_k. Flow field snapshots can be reassembled into matrices X and X'. Linear DMD is capable of identifying the optimal linear operator that evolves X into X'

$$X' \approx AX \quad \left(x_{k+1} = Ax_k\right) \tag{4}$$

When the state dimension n is exceedingly large, directly handling the complete $A \in \mathbb{R}^{n\times n}$ becomes less feasible. The DMD algorithm substitutes the full snapshot matrix with a matrix $A \in \mathbb{R}^{r\times r}$ mapped through POD, where r represents the reduced order dimension. The entire matrix is obtained through the singular value decomposition of X

$$X \approx U\Sigma V^* \tag{5}$$

where * denotes the conjugate transpose, and $U \in \mathbb{C}^{n\times r}$, $\Sigma \in \mathbb{C}^{r\times r}$, $V \in \mathbb{C}^{m\times r}$. The left singular vector $\mathbf{U}$ represents the POD modes. Since the columns of $\mathbf{U}$ are orthogonal, $\mathbf{U}*\mathbf{U} = I$. Similarly $\mathbf{V}*\mathbf{V} = I$. Thus, the matrix $\tilde{A}$ can be expressed as

$$\tilde{A} = U^* A U = U^* X' V \Sigma^{-1} \tag{6}$$

The next step involves the eigenvalue decomposition of matrix $\tilde{A}$

$$\tilde{A} W = W\Lambda \tag{7}$$

Herein, the columns of $W \in \mathbb{C}^{r\times r}$ are the eigenvectors, and $\Lambda \in \mathbb{C}^{r\times r}$ is a diagonal matrix containing the corresponding eigenvalues . It is evident that a periodic excitation signal is being utilized to advance the PIDMD framework. For illustrative purposes, the autonomous dynamical system will be transformed into its time-continuous equivalent form.

$$\frac{\mathrm{d}x}{\mathrm{d}t} = \tilde{A}_c x \tag{8}$$

After obtaining the flow field modes of each order based on the piDMD model, a sparsity-promoting algorithm is employed to filter the modes. The core of the algorithm lies in solving the following optimization problem:

$$\min_{\alpha} \left(\mathcal{J}(\alpha) + \gamma \sum_{i=1}^{r} |\alpha_i| \right) \tag{9}$$

where α_i is the modal amplitude, represents the sparsity regularization parameter. For a detailed introduction to the SPDMD model, refer to Jovanović et al. [49]. The working diagram of the functioning of the pi-SPDMD model is shown in Figure 2.

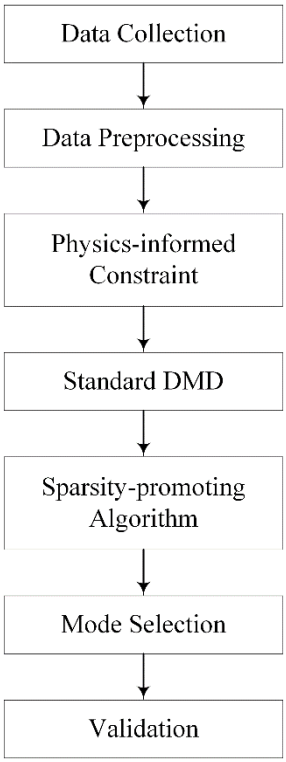

Fig. 2. The working diagram of the pi-SPDMD model.

3.3 Computational domain and mesh details

The computational domain comprised a cylinder, 10D in diameter, extending 2.5D upstream and 15D downstream from origin O, the propeller rotation center. A no-slip condition was applied to the propeller surface, uniform incoming velocity was imposed at the inlet, zero normal second derivative was designated for the outlet, and a slip-wall condition was enforced on the lateral cylindrical boundary. The rotation of the complete propeller is achieved through the overset grid technique. An annular tip refinement in cylindrical form, combined with a cylinder hub refinement stretching 9D downstream, is employed to adeptly delineate both tip and hub vortices from proximate to extended fields, as illustrated in Figure 3. The wall grid maintains a spacing where $y+ < 1$ at solid boundaries. The grid surrounding the propeller blades and hub is depicted in Figure 4. It is discernible from the figure that the geometric shape of the propeller is accurately represented by high-quality prismatic boundary layer grids. The prismatic layer grid strikes a balance between tetrahedral and hexahedral grids, demonstrating a high degree of automatic grid division and effective shear layer representation. This advantageous for solving the near-field flow around the propeller. The entire domain comprises roughly 82.5 million cells. Wall-proximate meshing is refined to a dimension of 0.000016m, while the core flow's minimum grid size for the tip and hub vortices is 0.0015m. Each cell's maximum skewness is kept under 9.5, and the peak non-orthogonality does not exceed 80. The Courant number remains between 0 and 1, with the highest values found in the finely-gridded hub vortex region.

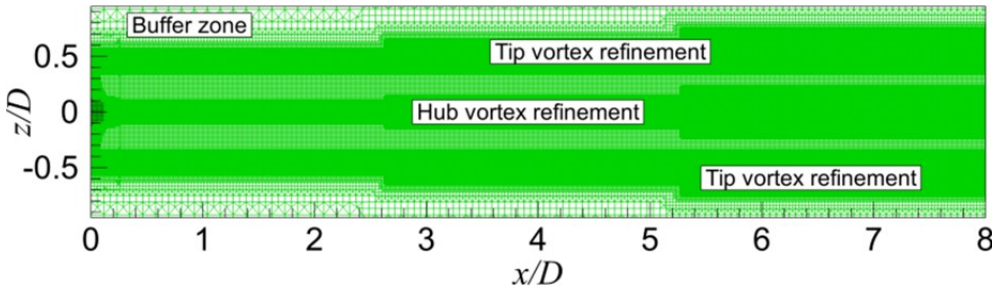

Fig. 3. Mesh distribution with wake refinements including tip vortex refinement and hub vortex refinement.

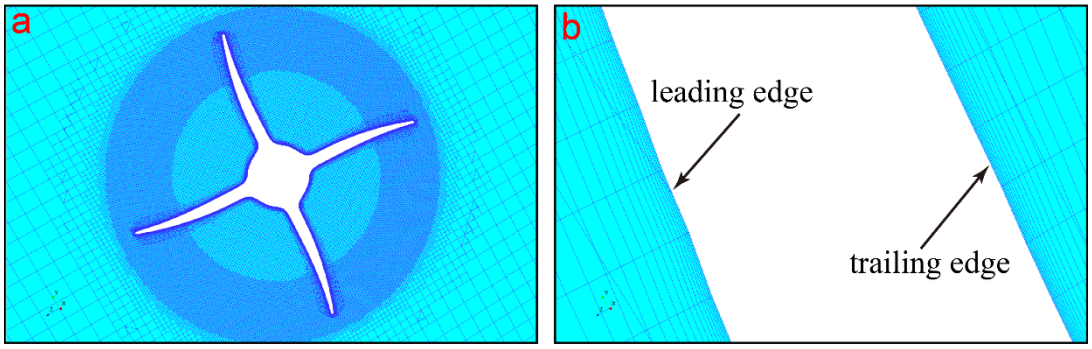

Fig. 4. Mesh distribution around (a) propeller blade and (b) propeller hub.

3.4 Numerical validation

In the CFD simulations analyzing open-water characteristics, results are benchmarked against experimental data from existing literature. Thrust and torque coefficients, Kt and Kq, as well as propeller efficiency η are derived as

$$Kt = \frac{T}{\rho n^2 D^4} \tag{10}$$

$$Kq = \frac{Q}{\rho n^2 D^5} \tag{11}$$

$$\eta = \frac{Kt}{Kq} \cdot \frac{J}{2\pi} \tag{12}$$

where T and Q are the propeller thrust and torque, respectively, ρ is the fluid density, n denotes the propeller rotational speed, D stands for the propeller diameter and J is the advance coefficient.

Figure 5a delineates a comparison between CFD-derived open-water characteristics and their corresponding experimental values. The CFD outcomes correspond closely with the empirical observations of Salvatore et al. [50].

Based on the phase-averaged physical quantity defined in Equation (13), Figure 5b depicts the non-dimensional axial velocity comparison, where the profile was extracted at x/D=0.1 on a line from the propeller hub center to the tip vortex.

$$\langle f \rangle (x,y,z) = \frac{1}{N} \sum_{i=1}^{N} f\left(x,y,z,t_0 + \frac{i-1}{mn}\right) \tag{13}$$

given $\langle f \rangle$ represents the phase-averaged value, with N as the total count of instantaneous flow fields where propeller blades traverse the same azimuthal position, t_0 marking the initiation of sampling post full flow development, and m signifying the total blades on the propeller. The CFD results align well with the data presented in Di Felice et al. [25].

The aforementioned assessment corroborates the numerical strategy employed in this study, suggesting the modeling technique and selected grid system are apt for investigating the origins of propeller-wake instability.

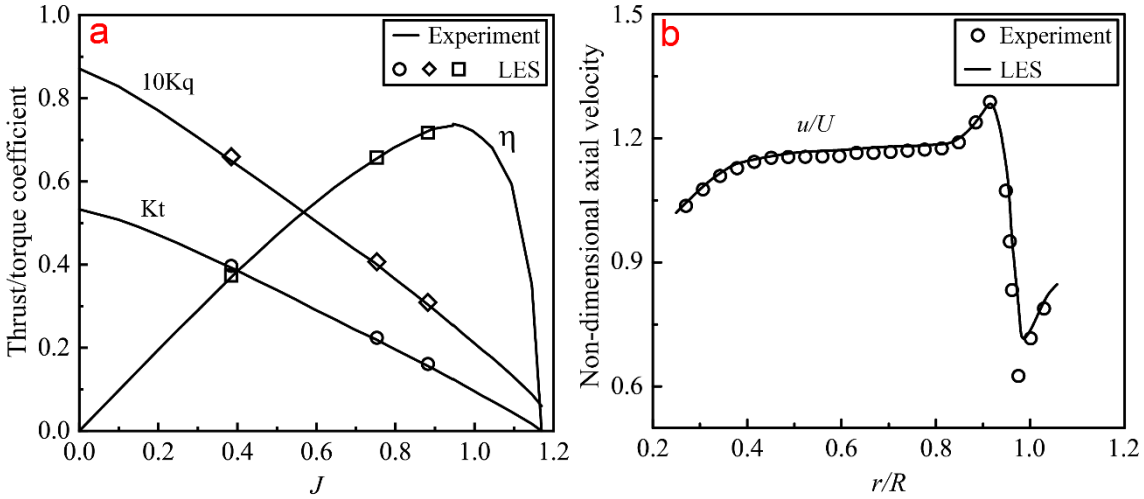

Fig. 5. Comparative analysis of LES and experimental outcomes: (a) open-water attributes and (b) phase-averaged axial velocity at J = 0.88.

4. Results and analysis

Figure 6 presents the three-dimensional vortex system aft of the propeller, computed based on the current discretization method and the numerical model, and is depicted using iso-surface of the *Q*-Criterion. Within the vortex system, the tip vortices and hub vortices are comparatively strong, while other vortex structures of the present propeller, such as root vortices and trailing edge vortices, are relatively weak and cannot persist in the wake. The tip vortices, shed from the four blades, evolve from the near to far field in a helical shape, and exhibit an instability behavior of adjacent tip vortex pairing downstream. The hub vortex, shed from the propeller hub, maintains good coherence throughout its evolution, displaying a stable vortex structure. Notably, the pairing process of the tip vortices downstream is accompanied by an instability of the tip vortex topological structure itself, manifesting as elliptical instability progressively developing on its surface.

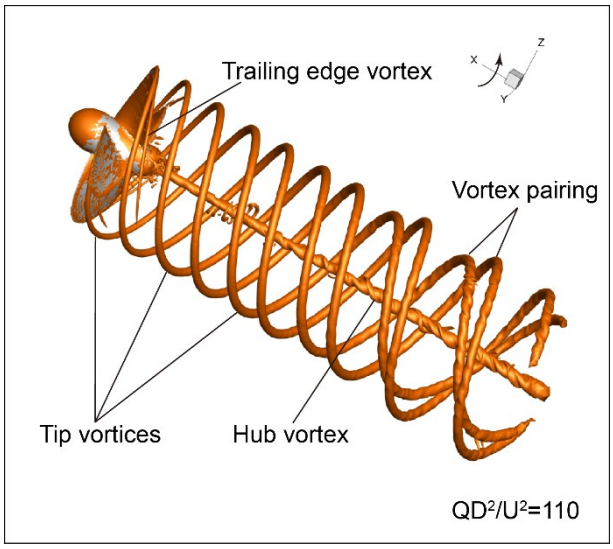

Fig. 6. The instantaneous three-dimensional vortex system behind the propeller represented by the iso-surface of *Q*=110.

Figure 7 delineates the wake characteristics of the blade, showcasing the instantaneous physical quantities at *r/R* = 0.9. Kinetic energy (KE) is given by $KE = 0.5\left(u^2 + v^2 + w^2\right)$. It can be observed that the rotational motion of the propeller exerts negligible influence on its own incoming flow, which is consistent with the findings presented in Kumar and Mahesh [30]. In the near field, as the blade moves, flow acceleration becomes apparent, leading to a pressure differential between the pressure and suction facets, which produces

its propulsive force. The blade wake exhibits areas with reduced axial velocity, increased vorticity, and enhanced kinetic energy at regular Radial intervals, appearing inclined within this field. In both the wake transition and far field regions, alternating bands of robust and faint tip vortices emerge due to field diffusion. Turbulent structures that connect neighboring tip vortices form, leading to the emergence of discretized vortex patterns. Consequently, this causes the swift degradation of the tip vortex, culminating in an isotropic flow field in the transition and far field regions.

Figure 8 represents the distribution of instantaneous velocity and pressure fields on the central longitudinal section, and the distribution of pressure and velocity ahead of the propeller also indicates that the propeller itself has no influence on its inflow. The streamwise velocity is larger at the inner radius, where the vortex structures migrate more rapidly. The distribution of the streamwise velocity and pressure fields downstream of the propeller further demonstrates the evolution process of the wake system from stable to unstable, specifically manifested as the flow field topology representing vortex structures in the near-field being highly regular. The instability of the wake more closely resembles a transition from a concentrated distribution of relevant physical quantities to a dispersed one, accompanied by strong flow mixing and radial expansion of the wake, which is even more pronounced in the far field.

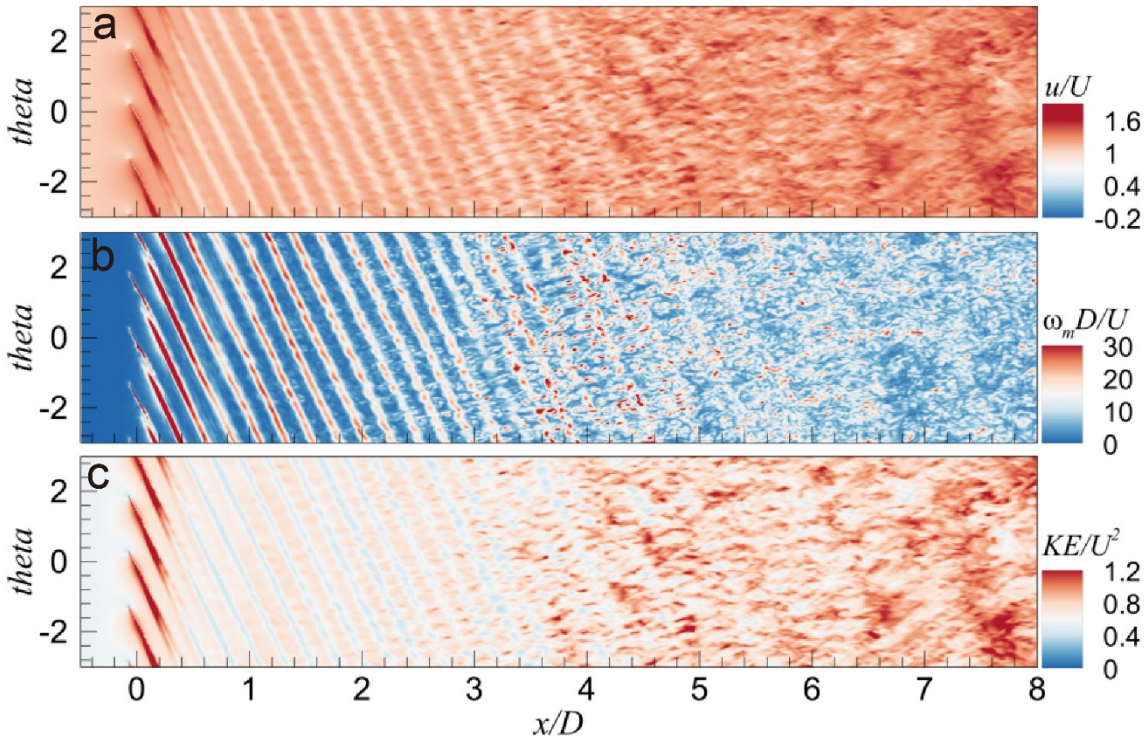

Fig. 7. The instantaneous flow fields on the x-θ surface at r/R = 0.9: (a) streamwise velocity scaled by U, (b) vorticity magnitude scaled by U/D, and (c) kinetic energy scaled by U^2.

Several probes, labeled as P_i (i=1–9), are positioned in the downstream wake to evaluate the kinetic energy and pressure over varying downstream distances in the time domain. Thereby offering a detailed understanding of the propeller wake evolution [51-56]. To delve deeper into the flow dynamics of tip vortices, the probes are strategically positioned at axial locations x/D = 0.4, 0.8, 1.2, 3.2, 3.6, 4.0, 7.0, 7.4, and 8.0 and radial locations r/R = 0.9, 0.9, 0.88, 0.87, 0.87, 0.87, 0.92, 0.92, and 1.02. The sketch of probe arrangement is shown in Figure 9, where probes are located along the tip vortex trajectory and the wake expansion in the downstream is taken into account. Figure 10 showcases box plots representing kinetic energy and pressure as recorded by these representative probes, highlighting both the mean values and fluctuations across various probe locations.

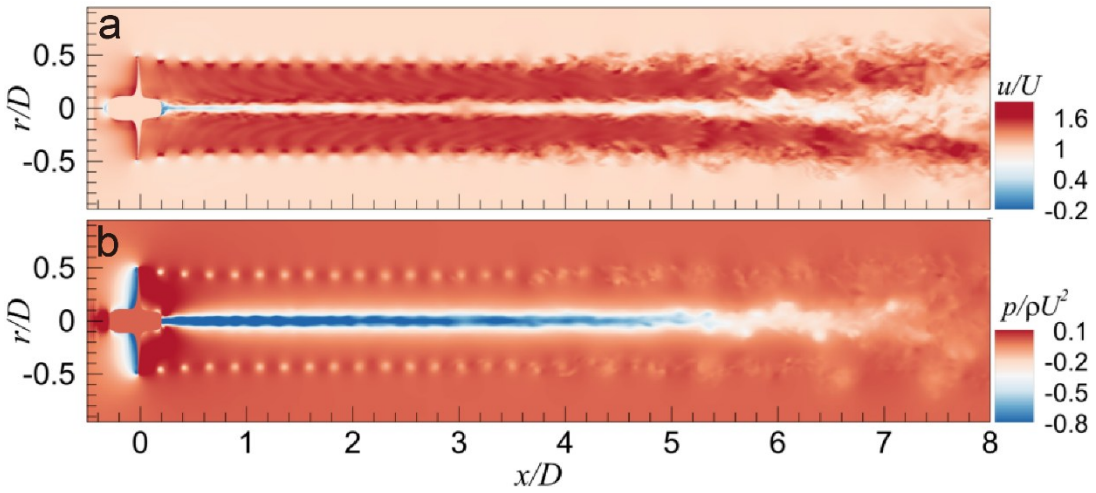

Fig. 8. The instantaneous flow fields on the longitudinal plane: (a) streamwise velocity scaled by U and (b) pressure scaled by ρU^2.

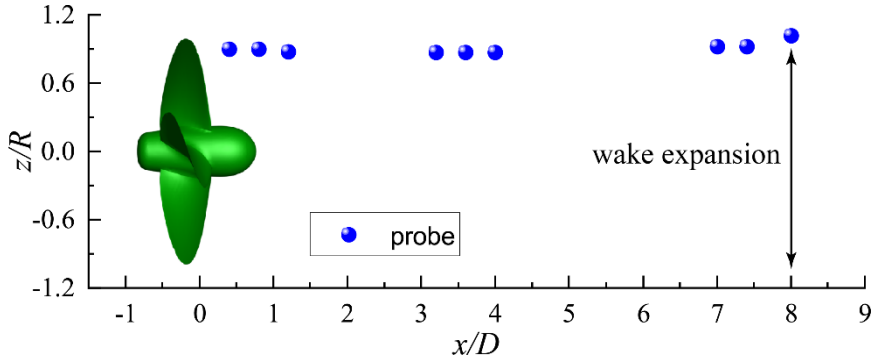

Fig. 9. Sketch of probe arrangement in the propeller wake.

Generally, as the distance downstream increases, both the mean values of kinetic energy (KE) and pressure decline, signifying the wake energy attenuation throughout its downstream progression. The diminution in the mean KE is subtle, with a more pronounced reduction observed initially when the tip vortex begins to lose its coherence. Fluctuations in KE and pressure exhibit distinct patterns across downstream probes. KE fluctuations are notably pronounced at points P_1 and P_3, attributed to the stability of the near-field wake. In the mid-field, probes P_4 and P_6 display oscillations arising from the destabilization of the tip vortex. Conversely, in the far field, the disintegration of the tip vortex contributes to reduced KE fluctuations at P_7 and P_9. Pressure fluctuations sharply wane as the distance downstream increases, a consequence of the tip vortex transitioning from a coherent structure to an array of uniformly dispersed small-scale vortices.

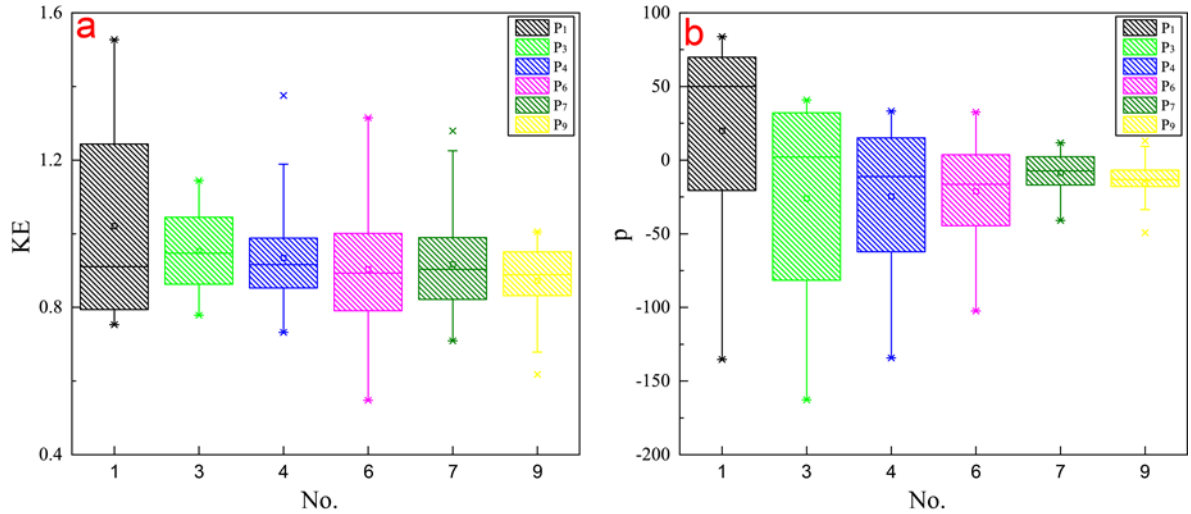

Fig. 10. Box plots represent the temporal fluctuations of kinetic energy (KE) and pressure across six downstream probes.

Intermittency is a salient characteristic of turbulence, denoting the alternating occurrence of turbulent and non-turbulent regions within a turbulent flow field. This intermittency profoundly affects the statistical properties of turbulence and its interaction with bounding walls. The aspect of intermittency in turbulence is paramount in numerous applications due to its impact on fluid transport properties, such as heat transfer, mass transfer, and momentum conveyance. To delve into the flow dynamics, we further analyze the turbulence statistics within propeller wakes. Figure 11 displays the PDFs for pressure and velocity, with σ denoting the standard deviation. The data is presented in a semi-logarithmic fashion, and the solid parabolic line serves as a reference, depicting a normalized Gaussian distribution.

From a physical perspective regarding velocity, pressure, and KE, the dynamics of the vortex wake can be conceptualized as a system requiring sufficient energy for stabilization. The downstream progression of this propeller wake system experiences energy depletion, primarily resulting from interactions among adjacent vortices. While the system energy in the near and middle fields suffices to uphold the vortex topology stability, the far field witnesses a rapid energy decline due to vortex structural interactions. This energy shortfall subsequently leads to the system vortex destabilization.

The most pronounced deviation is evident at probes located at x/D = 1 and 3. This is attributed to the dominance of large-scale vortexes in the propeller wake and the presence of coherent vortex structures in both the near and middle fields, underscoring a pronounced turbulence intermittency. This observation aligns with the data presented in Figure 7. Conversely, at the probe with x/D = 5, the PDFs for velocity and pressure fluctuations display a more subtle divergence from the Gaussian standard, suggesting an earlier disruption in the propeller wake and significant turbulent mixing.

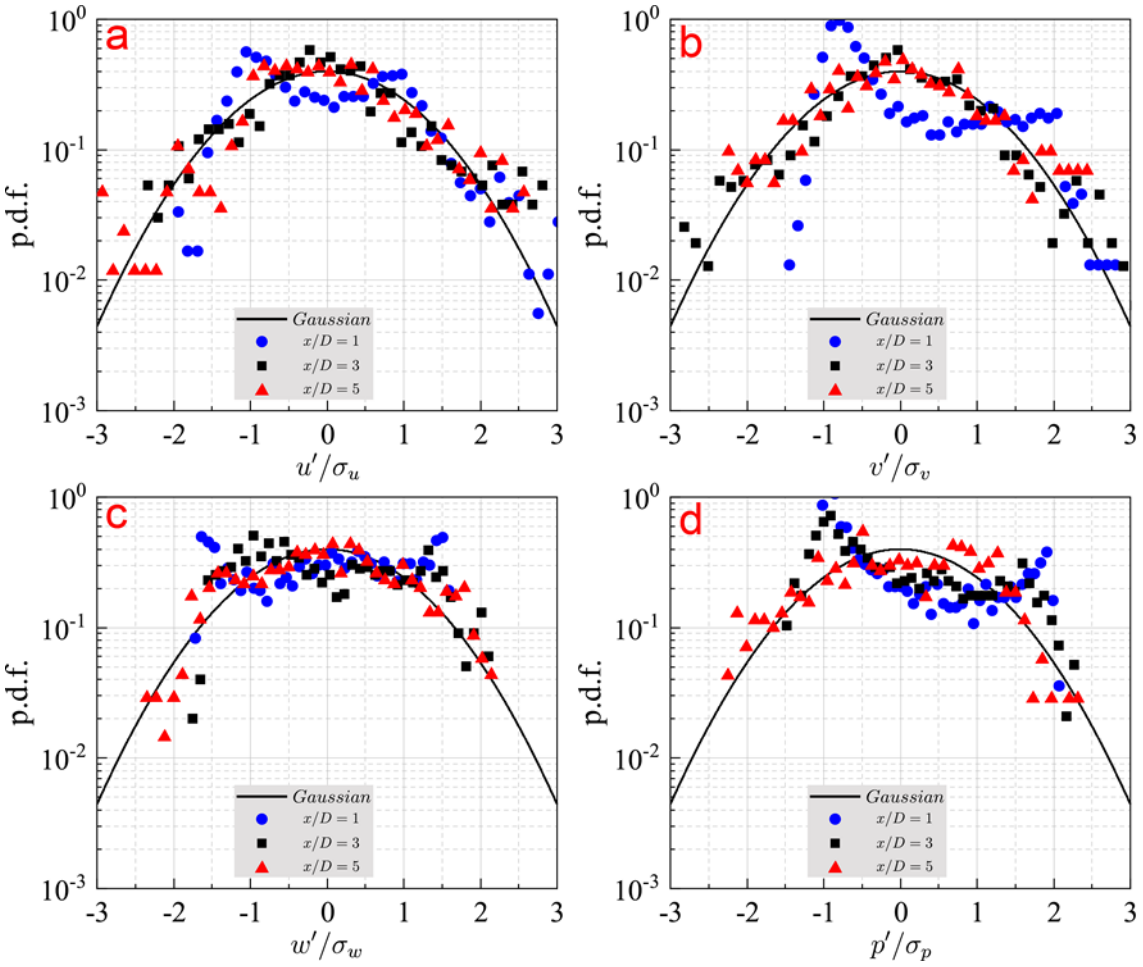

Fig. 11. PDFs of the fluctuations in (a) streamwise, (b) horizontal, (c) vertical velocities, and (d) pressure at downstream probes. σ signifies the standard deviation of the respective flow metric.

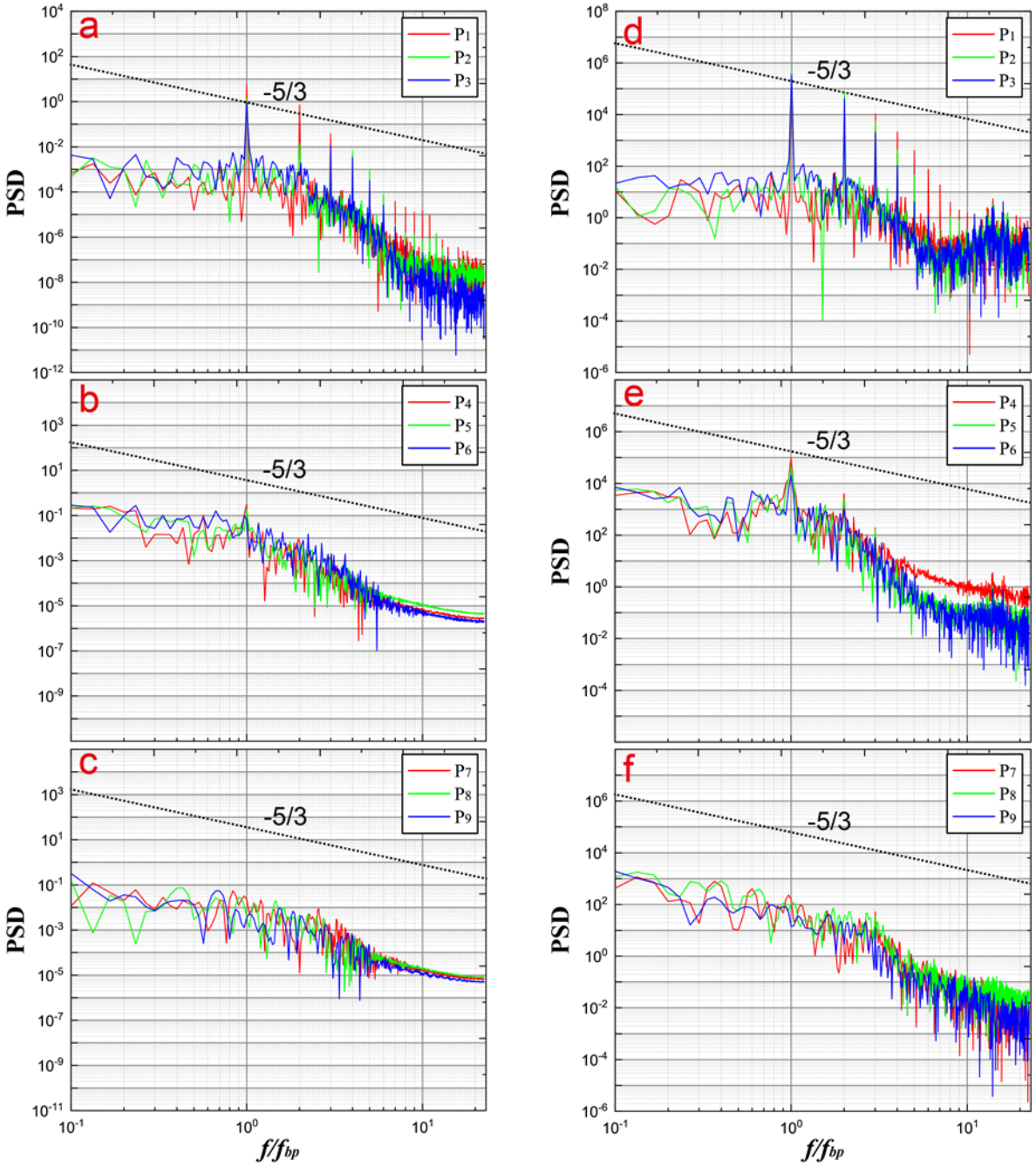

Fig. 12. The power spectral densities for the time-evolved kinetic energy (a, b, c) and pressure (d, e, f) are presented across nine downstream probes. The horizontal axis is normalized by the blade passage frequency, f_{bp}.

Examining the energy-transfer process, specifically through the PSD analysis of kinetic energy, provides insights into the wake system's evolutionary mechanism, as evidenced by various studies. This process, evident in the streamwise development of the kinetic energy's PSD, suggests an energy redistribution based on fundamental frequencies. Figure 12 showcases the PSDs for both kinetic energy and pressure across nine downstream probes. Notably, the present numerical simulation aligns with the anticipated -5/3 slope of the Kolmogorov theory's inertial range across multiple scales.

Within the stable wake of the near field, the average PSD amplitude is highest at point P_3, followed by P_2, and then P_1 across the full frequency range. This sequential decline is not evident in the mid-field and far-field, regions where tip-vortex instability manifests. In both the near and mid-fields, pronounced peaks are evident at the blade passage frequency (f_{bp}) and its harmonics. For points P_1, P_2, and P_3, the predominant peaks align with the blade frequency. Yet, for downstream probe P_4 in the mid-field, the primary peak transitions to

$0.5f_{bp}$, signifying the onset of tip vortex instability. The PSDs at P_7-P_9 present no significant peaks, demonstrating that the tip vortices lost coherence and tend to homogeneous distribution.

In computational fluid dynamics, the application of modal decomposition techniques is extensive. This methodology decomposes intricate flow field data into various modes or patterns, facilitating a more profound understanding and analysis of the characteristics of fluid flow. The data generated by computational fluid dynamics simulations is typically voluminous, encompassing a plethora of details. Modal decomposition facilitates the segmentation of this data into a series of modes, where each mode represents flow field characteristics at distinct scales or frequencies. This aids researchers in reducing data dimensionality, eliminating superfluous information, and better comprehending the primary attributes of the flow field. Modal decomposition techniques play a pivotal role in vortex analysis, noise assessment and control, flow field interpolation and reconstruction, as well as turbulence modeling and prediction.

In this study, 1800 radial velocity snapshots on the x/D=0.4 cross-section were selected for modal analysis, corresponding to the computational results over 10 rotations of a propeller in the numerical simulation. Each snapshot represents the transient flow field for every two time steps, and is obtained through interpolation from the original flow field, that is, data on the non-uniform grid in CFD calculations are interpolated onto a uniform structured grid as input data for modal decomposition. Based on previous research [57], the sampling frequency adheres to the Nyquist-Shannon criterion [58-59].

Figure 13 presents the distribution of eigenvalues derived from various modal analysis models. The white dashed line in the figure represents the unit circle, while the green crosses indicate the modes selected using the sparse-promoting approach from both the standard DMD method (denoted as SPDMD) and the piDMD method (denoted as pi-SPDMD). The modal eigenvalues manifest in the form of conjugate complex pairs, and they are symmetrically distributed with respect to the horizontal axis. These conjugate modes possess identical stability characteristics and frequencies, differing only in the sign of the frequency. Therefore, the mode corresponding to the positive frequency can represent the characteristics of this pair of modes. In Figure 13(a), the black hollow circles represent modes computed using the standard DMD method. It is evident that the majority of these circles are situated on the unit circle, indicating that the modes are stable and do not change over time. A minority of the circles are located within and near the unit circle, suggesting that these modes exhibit a growing trend over time. The figure also indicates that the motion of the propeller wake is periodic. In Figure 13(b), the black hollow circles represent the modes computed using the piDMD method. As observed from the figure, all modal eigenvalues are situated on the unit circle, denoting that all modes are stable at this instance. This suggests that the pi-SPDMD method offers certain advantages in modal analysis, specifically its ability to yield inherently stable modes.

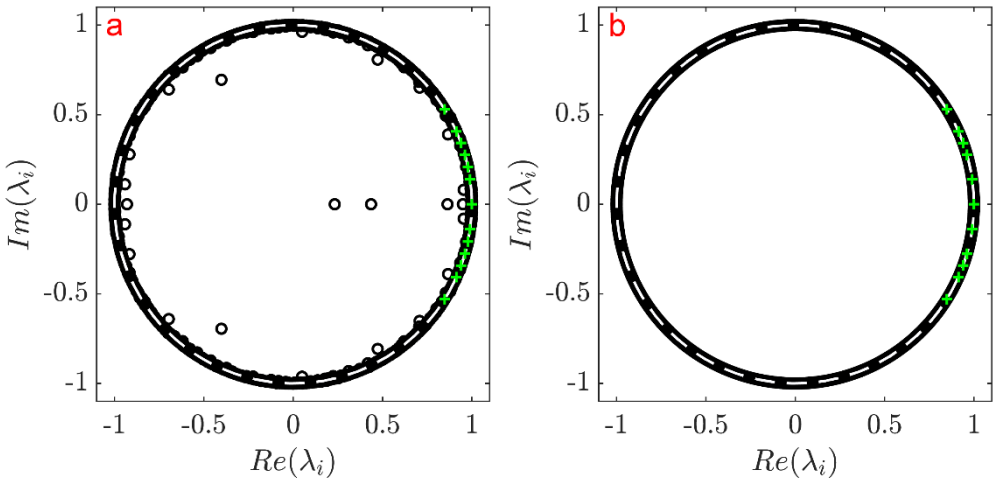

Fig. 13. Distribution of eigenvalues for (a) SPDMD and (b) pi-SPDMD

Figure 14 shows the functional relationship between the performance loss obtained from modal decomposition using two modal analysis models, the number of retained modes, and the relationship between the number of retained modes and sparse parameters. In general, regardless of which model is used, the fewer

the number of retained modes, the greater the performance loss. This can be understood because when all modes are used to reconstruct the original flow field, there will be no performance loss, and the larger the sparse parameter, the fewer the retained modes. By comparing the results of the two modal decomposition models, it can be seen that pi-SPDMD still has excellent performance loss even when retaining fewer modes, as shown in Figure 14(a). This indicates that the flow field modes obtained from the pi-SPDMD model decomposition have better physical fidelity under the same number of conditions. From Figure 14(b), it can be observed that compared to the SPDMD model, the pi-SPDMD model can quickly obtain sparser results as the sparse parameter increases, which to a certain extent improves the efficiency of the sparsity-promoting algorithm.

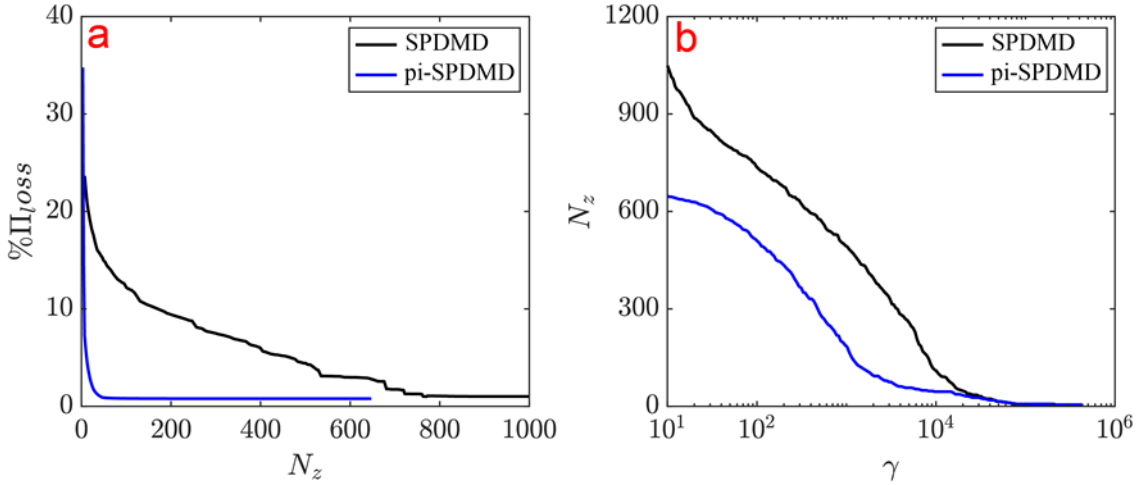

Fig. 14. Modal decomposition results for (a) the performance loss versus the number of retained modes and (b) the number of retained modes versus the sparsity regularization parameter

Figure 15 presents the relationship between modal amplitude and modal frequency as calculated using different modal decomposition models. It is evident that the modal amplitude is symmetrically distributed about the zero-frequency axis. Historically, researchers often ranked and selected modes based on modal amplitude or modal energy. However, in this study, the most representative modes were chosen based on a sparsity-promoting algorithm, aiming to achieve an optimal balance between the number of modes and performance loss. The blue crosses in the figure represent modes selected from the standard DMD and piDMD results, revealing that the selected modes are not necessarily those with the highest amplitude. Comparing the results from the SPDMD decomposition with those of the pi-SPDMD, there is a noticeable difference in the shape of their modal amplitude distributions.

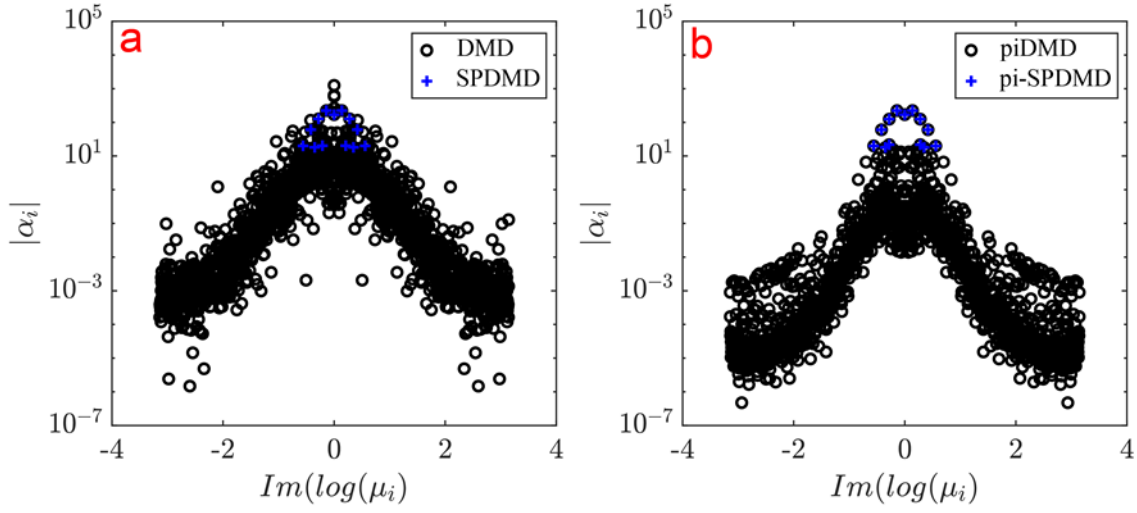

Fig. 15. Amplitude and frequency for (a) SPDMD and (b) pi-SPDMD

Figure 16 illustrates the relationship between modal frequency and modal growth rate as calculated using different modal decomposition models. In the figure, the color represents the modal amplitude, with modal points symmetrically distributed about the horizontal zero-frequency axis. Notably, for both models, the majority of modes are centered where the growth rate is zero, indicating that the propeller wake is stable and periodic. Comparing the results of SPDMD and pi-SPDMD, it is evident that all modes derived from the latter are distributed near zero frequency, suggesting that the pi-SPDMD model aptly preserves the physical properties of the original flow field. It's essential to emphasize that zero frequency represents a special case corresponding to time-averaged flow, and this study does not analyze modes at this frequency.

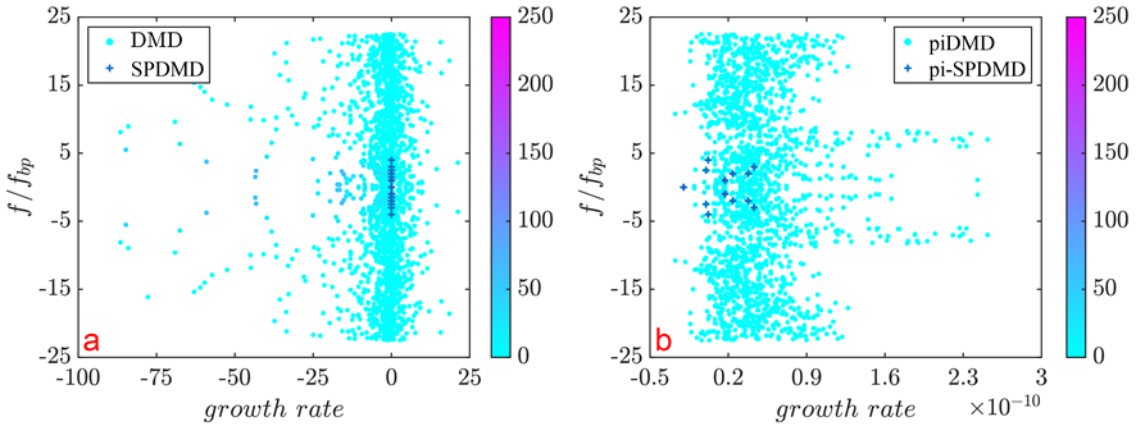

Fig. 16. Growth rate and frequency for (a) SPDMD and (b) pi-SPDMD

Figure 17 illustrates the first six modal structures of the radial velocity field at the section of x/D=0.4, obtained using the SPDMD method. It is discernible from the figure that modes corresponding to high frequencies present small-scale flow structures, while those associated with low frequencies exhibit large-scale flow patterns. The modal structures derived using the SPDMD method all manifest strong coherence. On the current cross-section, the modality of the radial velocity indicates a pronounced coherence in the azimuthal direction, which is consistent with the actual distribution of radial velocity in flow. Each modal order distinctly represents the flow structures within the wake system, indicative of tip vortices, trailing-edge vortices, and hub vortices, and their interconnected topological relations. Mode 1 depicts how the hub vortex in the vortex system is interconnected with the corresponding tip vortex via the trailing-edge vortex, collaboratively forming a stable wake vortex system. Mode 2 reveals the interference between the trailing-edge vortex and tip vortex leading to an alteration in their topological structures, with the trailing-edge vortex exhibiting rapid instability. This instability is associated with the high streamwise velocity at the inner radius, which disrupts the stable vortex system observed in Mode 1. Mode 3 presents the transformation in the topological structure of the tip vortex following the complete breakdown of the trailing-edge vortex, signifying some azimuthal and radial diffusion. Mode 4 demonstrates that the initial dissipation of the trailing-edge vortex system is accompanied by the azimuthal diffusion of the tip vortex structure. Modes 5 and 6 highlight the close link between the mutual induction effects of the tip vortex and the significant azimuthal diffusion of its structure triggered by instability, with both phenomena reinforcing each other.

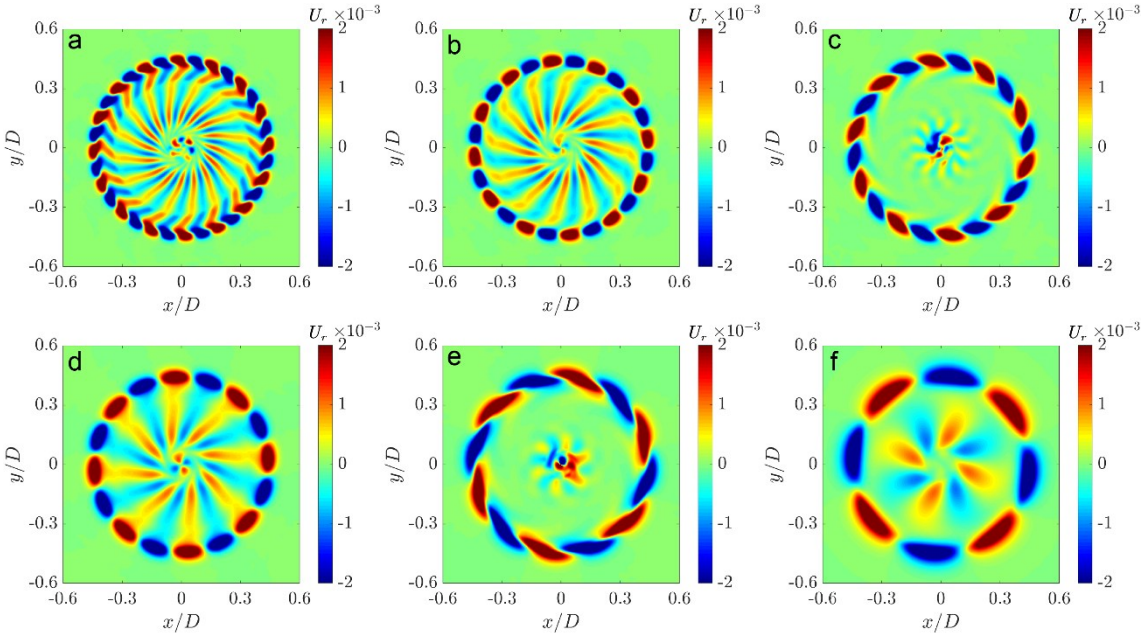

Fig. 17. The first six modes of SPDMD for (a) mode 1, f/f_{bp}=4, (b) mode 2, f/f_{bp}=3, (c) mode 3, f/f_{bp}=2.5, (d) mode 4, f/f_{bp}=2, (e) mode 5, f/f_{bp}=1.5, (f) mode 6, f/f_{bp}=1

Figure 18 presents the first six modal structures of the radial velocity field at the x/D=0.4 section, derived using the pi-SPDMD method. Upon comparison with Figure 17, it is evident that some modes obtained from pi-SPDMD share the same frequency as those from SPDMD, and their corresponding modal structures are nearly identical. A notable difference is that the former identifies two modes with a frequency of 2, namely Mode 4 and Mode 5, of which Mode 4 does not appear in the decomposition results of SPDMD. This suggests that pi-SPDMD incorporates the physical attributes of the flow field in its modal decomposition and selection. Mode 4 presents a flow structure that lacks coherence, contrasting with the coherence observed in all the first six modes in Figure 17. This indicates that the propeller wake system inherently possesses unstable components, which manifest as azimuthal diffusion, mixing, and small-scale flow structures.

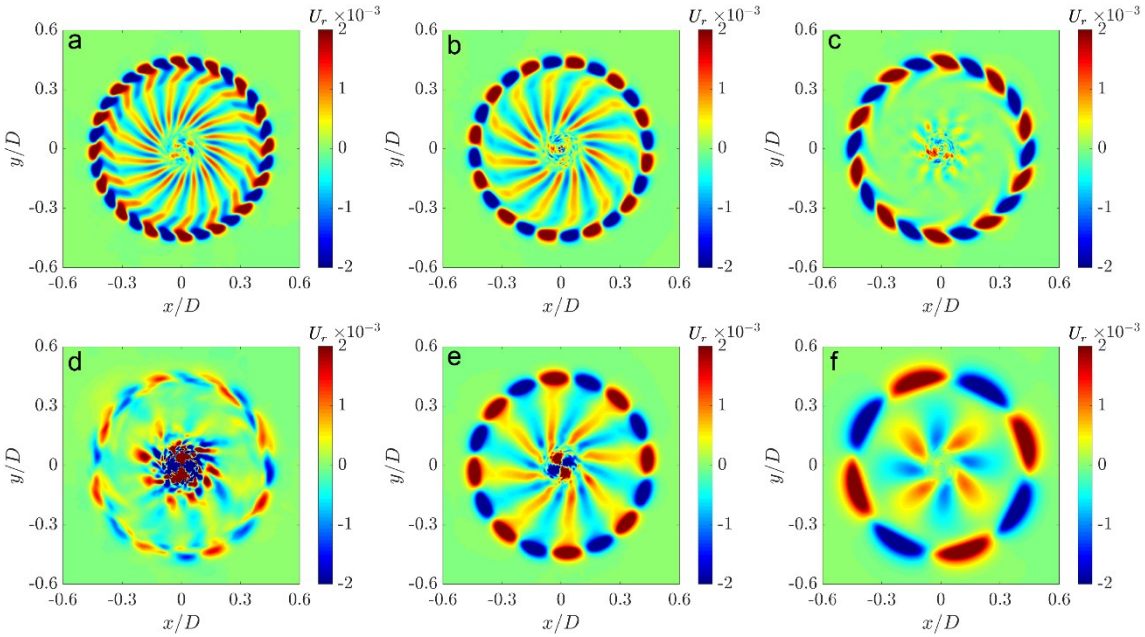

Fig. 18. The first six modes of pi-SPDMD for (a) mode 1, f/f_{bp}=4, (b) mode 2, f/f_{bp}=3, (c) mode 3, f/f_{bp}=2.5, (d) mode 4, f/f_{bp}=2, (e) mode 5, f/f_{bp}=2, (f) mode 6, f/f_{bp}=1

Taking into account both accuracy and efficiency, the first six modal structures shown in Figures 17 and 18 are employed to reconstruct the propeller wake field. The radial velocity field is reconstructed at a specific instance. The reconstructed flow field at any given time can be calculated using the following equation:

$$v_i^{rec} = \sum_{j=1}^{N-1} \varphi_j \left(\mu_j\right)^{i-1} \alpha_j \tag{14}$$

where v_i^{rec} represents the reconstructed velocity field, φ_j is the flow mode, α_j is the mode amplitude and μ_j is the eigenvalue. The reconstruction error is utilized to evaluate the quality of the flow field reconstruction. The reconstruction error at the i^{th} grid node can be calculated using the subsequent equation:

$$\text{Error}\left(\text{rec}_i\right) = \frac{\left|v_i^{\text{CFD}} - v_i^{\text{rec}}\right|}{\left|v_i^{CFD}\right|} \times 100\% \tag{15}$$

Figure 19 presents a comparison between the flow fields reconstructed using modal structures obtained from different modal decomposition models and the original flow fields. Overall, the reconstructed flow fields align well with the original one, although some discrepancies are observed near the trailing-edge vortex structures. The reconstructed flow fields effectively capture the primary flow characteristics on the cross-section, such as the tip vortex, hub vortex, and trailing-edge vortex structures. Figure 20 displays the error contour diagram on each grid node of the cross-section, highlighting that the reconstruction errors are primarily localized near the trailing-edge vortex. The decomposition results from both models are capable of accurately reconstructing the tip vortex structures of comparable intensity. The relative reconstruction error between pi-SPDMD and SPDMD is also illustrated in Figure 20. It is evident that the former effectively enhances the reconstruction performance in the vortex region compared to the latter. However, both models still exhibit suboptimal reconstruction results in the trailing-edge vortex region. This observation suggests that further improvements in the pi-SPDMD model should prioritize addressing this specific region. This offers a potent tool for the numerical forecasting of propeller wake instability. Previously, the evolution of propeller wakes necessitated numerical simulations with high spatiotemporal resolutions and advanced turbulence models. However, now it may be possible to conduct relatively accurate forecasts and analyses based on reduced-order reconstruction techniques. It is worth noting that this study only examined the modal decomposition of two-dimensional flow fields on a fixed cross-section. The modal analysis of three-dimensional flows might still require hardware support.

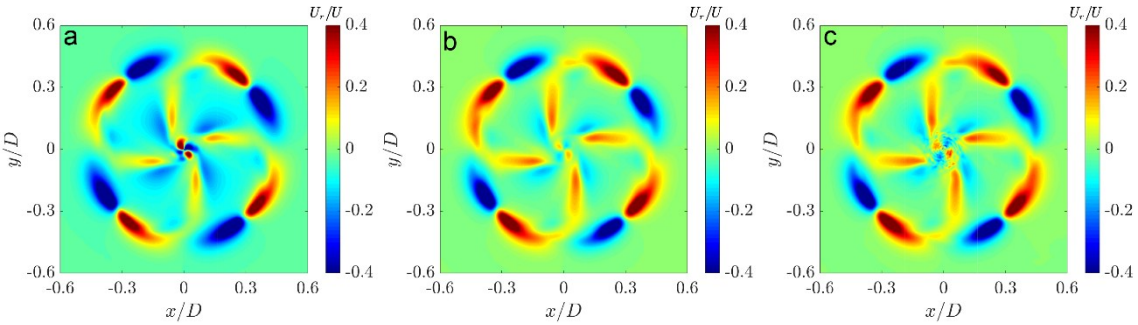

Fig. 19. The original and reconstructed non-dimensionalized radial velocity contours at x/D=0.4 for (a) CFD calculation, (b) the reconstruction of SPDMD and (c) the reconstruction of pi-SPDMD.

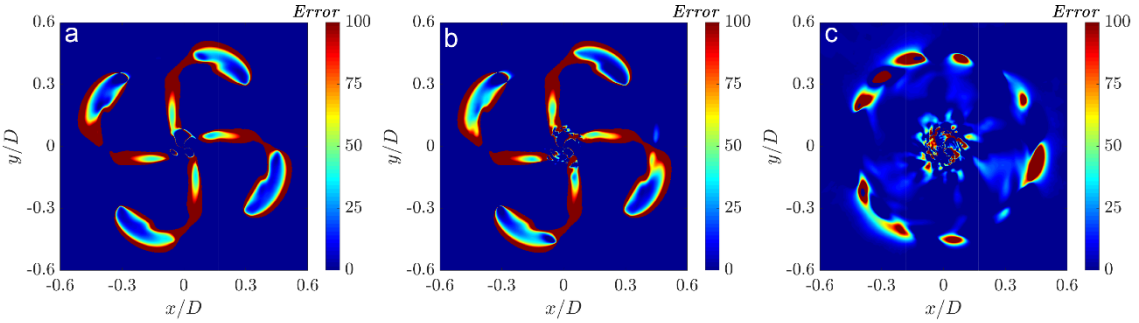

Fig. 20. The contours for (a) reconstruction error of SPDMD, (b) reconstruction error of pi-SPDMD and (c) relative reconstruction error between SPDMD and pi-SPDMD.

5. Conclusions

Over recent decades, there has been a growing focus on the intricate dynamics of propeller wakes and their extensive engineering implications. In this study, LES is employed to capture the nuanced wake development of a four-bladed propeller. A new modal analysis approach, named the pi-SPDMD, has been introduced to streamline and reconstruct intricate propeller wake flows, thereby shedding light on the inherent flow patterns across diverse time and space scales.

The results show that the pi-SPDMD model enhances the efficiency of the sparse-promoting algorithm, yielding modes that tend towards stability, and the decomposition results possess good physical fidelity. By integrating the LES solution and the modal decomposition results from pi-SPDMD, the tip vortex in the near field exhibits a stable structure characterized by distinct coherence. In this domain, the large-scale vortex is dominant, and turbulence intermittency is especially pronounced. By the mid-field, the wake vortex begins its transition into small-scale vortices and experiences a marked loss of coherence, attributed to the progression of elliptic instability and emergent secondary vortex structures. As this evolution persists downstream, the tip vortex engages with these secondary structures and adjacent tip vortices, culminating in the vortex system disintegration.

The current investigation enhances our understanding of the flow physics underlying tip vortex instability. Furthermore, it bolsters the advancement and refinement of high-performance propellers for future generations. The future work involves endeavoring to incorporate more physical constraints pertinent to specific flow conditions into the existing models. Furthermore, it is imperative to validate the effectiveness of these novel modal decomposition models in identifying significant structures in terms of time and spatial scales within fluid flows. Subsequent efforts will engage in the reconstruction and prediction of three-dimensional flow fields under intricate operating conditions, thereby contributing to both practical engineering and theoretical research pertaining to turbulent flows.

6. Acknowledgments

This work was supported by the Basic Research and Frontier Exploration Project of Chongqing (No. cstc2015jcyja30011).

REFERENCES

[1] Abbasi, A. A., Franzosi, G., Canepa, E., Gaggero, S., Villa, D., Viviani, M., Tani, G., 2023. Experimental analysis of the flow field around a propeller with inclined shaft. *Ocean Engineering*, 285, 115237. https://doi.org/10.2139/ssrn.4379651

[2] Belibassakis, K., Prospathopoulos, J., 2023. A 3d-BEM for underwater propeller noise propagation in the ocean environment including hull scattering effects. *Ocean Engineering*, 286, 115544. https://doi.org/10.1016/j.oceaneng.2023.115544

[3] D'Agostino, D., Diez, M., Felli, M., Serani, A., 2023. PIV Snapshot Clustering Reveals the Dual Deterministic and Chaotic Nature of Propeller Wakes at Macro-and Micro-Scales. *Journal of Marine Science and Engineering*, 11(6), 1220. https://doi.org/10.3390/jmse11061220

[4] Dinariyana, A. A. B., Deva, P. P., Ariana, I., Handani, D. W., 2022. Development of model-driven decision support system to schedule underwater hull cleaning. *Brodogradnja*, 73(3), 21-37. https://doi.org/10.21278/brod73302

[5] Wang, L., Guo, C., Wan, L., Su, Y., 2017. Numerical analysis of propeller during heave motion near a free surface. *Marine Technology Society Journal*, 51(1), 40-51. https://doi.org/10.4031/MTSJ.51.1.5

[6] Yurtseven, A., Aktay, K., 2023. The numerical investigation of spindle torque for a controllable pitch propeller in feathering maneuver. *Brodogradnja*, 74(2), 95-108. https://doi.org/10.21278/brod74205

[7] Zhi, Y., Qiu, R., Huang, R., Wang, Y., 2023. Dynamic mode decomposition and reconstruction of the transient propeller wake under a light loading condition. *Ocean Engineering*, 269, 113532. https://doi.org/10.1016/j.oceaneng.2022.113532

[8] Dogrul, A., 2022. Numerical prediction of scale effects on the propulsion performance of Joubert BB2 submarine. *Brodogradnja*, 73(2), 17-42. https://doi.org/10.21278/brod73202

[9] Di Felice, F., Capone, A., Romano, G. P., Pereira, F. A., 2023. Experimental study of the turbulent flow in the wake of a horizontal axis tidal current turbine. *Renewable Energy*, 212, 17-34. https://doi.org/10.1016/j.renene.2023.04.128

[10] Gaggero, S., 2023. A Study on the Wake Evolution of a Set of RIM-Driven Thrusters. *Journal of Marine Science and Engineering,* 11(9), 1659. https://doi.org/10.3390/jmse11091659

[11] Liang, L., Baoji, Z., Hao, Z., Hailin, T., Weijie, W., 2023. Hydrodynamic performance optimization of marine propellers based on fluid-structure coupling. *Brodogradnja*, 74(3), 145-164. https://doi.org/10.21278/brod74308

[12] Xu, S., Xiong, Y. L., Li, G. B., Wei, M. Y., Long, X. P., Ji, B., 2023. Investigation on the flow characteristics near the duct of a pump-jet propulsion under different advance coefficient conditions. *Ocean Engineering*, 285, 115304. https://doi.org/10.1016/j.oceaneng.2023.115304

[13] Guo, C. Y., Wang, L. Z., Zhao, Q. X., Wu, T. C., 2015. Approach of Ship Resistance Prediction with Consideration of Hull Gesture. *Ship Engineering*, 37, 31-34.

[14] Guo, C. Y., Xu, P., Wang, L. Z., Luo, W. Z., 2018. Hydrodynamic performance analysis of podded propulsor under ice blockage condition. *Journal of Huazhong University of Science and Technology (natural science edition)*, 46(5), 41-46.

[15] Guo, C., Zhang, D., Wang, L., 2019. Numerical simulation of propeller ventilation near the free surface. *Journal of Huazhong University of Science and Technology (Nature Science Edition)*, 47(2), 81-86.

[16] Guo, C. Y., Xu, P., Wang, C., Wang, L. Z., Zhang, C. S., 2020. Influence of ice size parameter variation on hydrodynamic performance of podded propulsor. *China Ocean Engineering*, 34(1), 30-45. https://doi.org/10.1007/s13344-020-0004-x

[17] Zhao, D., Guo, C., Su, Y., Wang, L., Wang, C., 2017. Numerical study on the unsteady hydrodynamic performance of a four-propeller propulsion system undergoing oscillatory motions. *Journal of Coastal Research,* 33(2), 347-358. https://doi.org/10.2112/JCOASTRES-D-16-00007.1

[18] Muscari, R., Di Mascio, A., Verzicco, R., 2013. Modeling of vortex dynamics in the wake of a marine propeller. *Computers and Fluids*, 73, 65–79. https://doi.org/10.1016/j.compfluid.2012.12.003

[19] Song, K. W., Guo, C. Y., Gong, J., Li, P., Wang, L. Z., 2018. Influence of interceptors, stern flaps, and their combinations on the hydrodynamic performance of a deep-vee ship. *Ocean Engineering*, 170, 306-320. https://doi.org/10.1016/j.oceaneng.2018.10.048

[20] Song, K., Guo, C., Sun, C., Wang, C., Gong, J., Li, P., Wang, L., 2021. Simulation strategy of the full-scale ship resistance and propulsion performance. *Engineering Applications of Computational Fluid Mechanics*, 15(1), 1321-1342. https://doi.org/10.1080/19942060.2021.1974091

[21] Wang, L., Martin, J. E., Carrica, P. M., Felli, M., Falchi, M., 2019. Experiments and CFD for DARPA Suboff Appended with Propeller E1658 Operating Near the Surface. *Proceedings of the 6th International Symposium on Marine Propulsors*, 26-30 May, Rome, Italy, 1-9.

[22] Wang, L., Martin, J.E., Felli, M., Carrica, P.M., 2020. Experiments and CFD for the propeller wake of a generic submarine operating near the surface. *Ocean Engineering*, 206, 107304. https://doi.org/10.1016/j.oceaneng.2020.107304

[23] Wang, L., Guo, C., Wang, C., Xu, P., 2021. Modified phase average algorithm for the wake of a propeller. *Physics of Fluids*, 33(3), 035146. https://doi.org/10.1063/5.0030829

[24] Wang, L., Liu, X., Wu T., 2022. Modal analysis of the propeller wake under the heavy loading condition. *Physics of Fluids*, 34(5), 055107. https://doi.org/10.1063/5.0088666

[25] Di Felice, F., 2004. Experimental investigation of the propeller wake at different loading conditions by particle image velocimetry. *Journal of Ship Research*, 48(02), 168-190. https://doi.org/10.5957/jsr.2004.48.2.168

[26] Felli, M., Camussi, R., Di Felice, F., 2011. Mechanisms of evolution of the propeller wake in the transition and far fields. *Journal of Fluid Mechanics*, 682, 5-53. https://doi.org/10.1017/jfm.2011.150

[27] Mukund, R., Kumar, A. C., 2016. Velocity field measurements in the wake of a propeller model. *Experiments in Fluids*, 57, 154. https://doi.org/10.1007/s00348-016-2237-2

[28] Felli, M., Falchi, M., 2018. Propeller wake evolution mechanisms in oblique flow conditions. *Journal of Fluid Mechanics*, 845, 520. https://doi.org/10.1017/jfm.2018.232

[29] Felli, M., Falchi, M., 2020. Propeller tip and hub vortex dynamic from the near to the very far field by time-resolved PIV measurements. *Proceedings of 33rd Symposium on Naval Hydrodynamics*, 18-23 October, Osaka, Japan, 136.

[30] Kumar, P., Mahesh, K., 2017. Large eddy simulation of propeller wake instabilities. *Journal of Fluid Mechanics*, 814, 361-396. https://doi.org/10.1017/jfm.2017.20

[31] Li, H., Huang, Q., Pan, G., Dong, X., 2021. Wake instabilities of a pre-swirl stator pump-jet propulsor. *Physics of Fluids*, 33, 085119. https://doi.org/10.1063/5.0057805

[32] Wang, L., Liu, X., Wang, N., Li, M., 2022. Modal analysis of propeller wakes under different loading conditions. *Physics of Fluids*, 34, 065136. https://doi.org/10.1063/5.0096307

[33] Posa, A., 2022. The dynamics of the tip vortices shed by a tip-loaded propeller with winglets. *Journal of Fluid Mechanics*, 951, A25. https://doi.org/10.1017/jfm.2022.852

[34] Posa, A., Broglia, R., Balaras, E., 2022. The dynamics of the tip and hub vortices shed by a propeller: Eulerian and Lagrangian approaches. *Computers & Fluids*, 236, 105313. https://doi.org/10.1016/j.compfluid.2022.105313

[35] Feng, D., Wang, X., Jiang, F., Zhang, Z., 2015. Large eddy simulation of DARPA SUBOFF for Re= 2.65× 107. *Journal of Coastal Research*, 73(spl), 687-691. https://doi.org/10.2112/SI73-118.1

[36] Mahesh, K., Constantinescu, G., Moin, P., 2004. A numerical method for large-eddy simulation in complex geometries. *Journal of Computational Physics*, 197(1), 215-240. https://doi.org/10.1016/B978-008044046-0.50009-9

[37] Posa, A., Broglia, R., 2022. Spanwise distribution of the loads on a hydrofoil working in the wake of an upstream propeller. *Ocean Engineering*, 264, 112542. https://doi.org/10.1016/j.oceaneng.2022.112542

[38] Posa, A., Broglia, R., Felli, M., Cianferra, M., Armenio, V., 2022. Hydroacoustic analysis of a marine propeller using large-eddy simulation and acoustic analogy. *Journal of Fluid Mechanics*, 947, A46, 1-33. https://doi.org/10.1017/jfm.2022.692

[39] Wang, T., Shi, H., Zhao, M., Zhang, Q., 2023. Effects of a nozzle on the propeller wake in an oblique flow using modal analysis. *Journal of Fluid Mechanics*, 959, A14. https://doi.org/10.1017/jfm.2023.111

[40] Li, S., Li, F., Huang, Q., Pan, G., Wang, S., Tian, X., 2023. On the space-time decomposition and reconstruction of the pump-jet propulsor flow field. *Ocean Engineering*, 286, 115521. https://doi.org/10.1016/j.oceaneng.2023.115521

[41] Wang, L., Guo, C., Xu, P., Su, Y., 2019. Analysis of the wake dynamics of a propeller operating before a rudder. *Ocean Engineering*, 188, 106250. https://doi.org/10.1016/j.oceaneng.2019.106250

[42] Wang, L., Wu, T., Gong, J., Yang, Y., 2021. Numerical analysis of the wake dynamics of a propeller. *Physics of Fluids*, 33(9), 095120. https://doi.org/10.1063/5.0064100

[43] Posa, A., 2023. Anisotropy of turbulence at the core of the tip and hub vortices shed by a marine propeller. *Journal of Fluid Mechanics*, 969, A23. https://doi.org/10.1017/jfm.2023.532

[44] Posa, A., Balaras, E., 2016. A numerical investigation of the wake of an axisymmetric body with appendages. *Journal of Fluid Mechanics*, 792, 470-498. https://doi.org/10.1017/jfm.2016.47

[45] Wang, C., Li, P., Guo, C., Wang, L., Sun, S., 2022. Numerical research on the instabilities of CLT propeller wake. *Ocean Engineering*, 243, 110305. https://doi.org/10.1016/j.oceaneng.2021.110305

[46] Posa, A., Broglia, R., Felli, M., Falchi, M., Balaras, E., 2019. Characterization of the wake of a submarine propeller via large-eddy simulation. *Computers and Fluids*, 184, 138-152. https://doi.org/10.1016/j.compfluid.2019.03.011

[47] Andredaki, M., Georgoulas, A., Marengo, M., 2020. Numerical investigation of quasi-sessile droplet absorption into wound dressing capillaries. *Physics of Fluids*, 32(9), 092112. https://doi.org/10.1063/5.0021828

[48] Nguyen, V. B., Do, Q. V., Pham, V. S., 2020. An OpenFOAM solver for multiphase and turbulent flow. *Physics of Fluids*, 32(4), 043303. https://doi.org/10.1063/1.5145051

[49] Jovanović, M. R., Schmid, P. J., Nichols, J. W., 2014. Sparsity-promoting dynamic mode decomposition. *Physics of Fluids*, 26(2). https://doi.org/10.1063/1.4863670

[50] Salvatore, F., Testa, C., Ianniello, S., Pereira, F., 2006. Theoretical modelling of unsteady cavitation and induced noise. *Proceedings of CAV 2006 Symposium*, Wageningen, Netherlands, 11-15 September, 1-13.

[51] Di Mascio, A., Muscari, R., Dubbioso, G., 2014. On the wake dynamics of a propeller operating in drift. *Journal of Fluid Mechanics*, 754, 263. https://doi.org/10.1017/jfm.2014.390

[52] Gong, J., Ding, J., Wang, L., 2021. Propeller–duct interaction on the wake dynamics of a ducted propeller. *Physics of Fluids*, 33(7), 074102. https://doi.org/10.1063/5.0056383

[53] Wang, L., Carrica, P.M., Felli, M., 2020. Experimental and CFD Study of the Streamwise Evolution of Propeller Tip Vortices. *Proceedings of 33rd Symposium on Naval Hydrodynamics*, 18-23 October, Osaka, Japan, 136.

[54] Wang, L., Wu, T., Gong, J., Yang, Y., 2021. Numerical simulation of the wake instabilities of a propeller. *Physics of Fluids*, 33(12), 125125. https://doi.org/10.1063/5.0070596

[55] Wang, L., Wu, T., Guo, C., 2021. Study on instability mechanism and evolution model of propeller tip vortices. *Chinese Journal of Theoretical and Applied Mechanics*, 53(8), 2267-2278.

[56] Wang, L., Liu, X., Wang, N., Li, M., 2022. Propeller wake instabilities under turbulent-inflow conditions. *Physics of Fluids*, 34(8), 085108. https://doi.org/10.1063/5.0101977

[57] Wang, L., Liu, X., Guo, J., Li, M., Liao, J., 2023. The dynamic characteristics in the wake systems of a propeller operating under different loading conditions. *Ocean Engineering*, 286, 115518. https://doi.org/10.1016/j.oceaneng.2023.115518

[58] Nyquist, H., 1928. Certain topics in telegraph transmission theory. *Transactions of the American Institute of Electrical Engineers*, 47(2), 617-644. https://doi.org/10.1109/5.989875

[59] Shannon, C. E., 1949. Communication in the presence of noise. *Proceedings of the IRE*, 37(1), 10-21. https://doi.org/10.1109/JRPROC.1949.232969